Journal of Data Acquisition and Processing
ISSN: 1004-9037
https://sjcjycl.cn/
DOI: 10.5281/zenodo.7641958

SEGMENTATION OF LUNG NODULES USING A GENERATIVE ADVERSARIAL NETWORK

Supiksha Jain[1], Sanjeev Indora[1], Dinesh Kumar Atal[2]
Department of Computer Science and Engineering1, Department of Biomedical Engineering[2]
Deenbandhu Chhotu Ram University of Science and Technology, Murthal, Sonipat, Haryana, India

Abstract-- The segmentation of lung nodules is an essential research area in the field of lung cancer detection, however achieving high accuracy is a major challenge due to the variability and distinctiveness of these nodules. In order to overcome this challenge, a generative adversarial network (GAN) model has been developed in the current study for lung nodule segmentation. Pre-processing methods, including the use of a Gaussian filter have been implemented to eliminate any artifacts that may have been present in the input computed tomography (CT) image. After pre-processing stage, the image has further aroused to lung lobe segmentation, which involved utilizing deep-joint segmentation techniques to accurately identify the relevant regions of the lung. GAN has been used to perform the lung nodule segmentation, with the model trained to segment lung nodules from the lung lobe image. Performance of the model has been evaluated using metrics namely accuracy, Jaccard-similarity, and Dice coefficient to assess its effectiveness.

Keywords: Lung lobe segmentation, Image pro-cessing, Lung nodule seg-mentation, Generative Adversarial-Network

Introduction

The primary cause of demise globally is Lung cancer. In advance, observation of lung cancer improves the chances of survival for those affected. Lung cancer has the highest cancer mortality rate. Delayed detection times can negatively impact the survival rate, with a higher likelihood of improved survival for cases of lung cancer that are detected earlier [1]. In order to diagnose lung cancer, CT imaging techniques are utilized to detect any unknown or suspicious nodules. However, the detection of cancer cells is challenging due to the complex anatomical structure of the lungs and the varying intensities present in CT scan images [2].

The term "lung nodule" refers to anomalies in lung tissue that manifest as spherical or round-shaped opacities. There are four main types of lung nodules: well-circumscribed, juxta-vascular, juxta-pleural, and pleural tails. These groups are differentiated by the nodule's connection with adjacent blood vessels [6].

Recent lung image segmentation CT researchers have focused on precise along with rapid segmentation procedures. Lung nodule segmentation procedures include thresholding methods, clustering, neural networks, morpho-logical methods, deformable models, graph cut method, active contours, water-shed, as well as histograms. [9], region growing [10], fuzzy logic-based segmentation. In [13], using Artificial Neural Networks (ANNs) to classify cancer in CT images is a widely adopted method. One feature used in this procedure is skewness, which has been found to significantly increase the accuracy of the classifier. The procedure has identical

grey values for the bronchus as well as for trachea but is not very powerful [14]. The integration of the kernel function with the BFC has been done to develop a kernel-based BFC for lung nodule segmentation. However, despite this approach, issues with accuracy arose due to the visual variations of nodules and heterogeneous present in lung nodules [8]. The segmentation process is influenced by familiarity with the visual features of the lung nodule as well as diversity of lung nodules [16]. DDRN procedure is used to identify nodules in CT images, but segmentation accuracy remains a significant challenge [17].

Literature review

In [18], proposed a technique that primarily utilizes a fix-based completely convolutional network (FCN) to restore discriminating squares and gives profound highlights with high effectiveness. At this point, distinctive setting mindful square selection and highlight accumulation methods are investigated to create an internationally all-encompassing WSI descriptor, which is finally adopted in an arbitrary Timberland classifier (RF) for picture-level prediction. Broad trials show the unrivalled exhibition of this technique, which outperforms best-in-class approaches by a critical edge with an exactness of 97.3%. The proposed technique achieves the best exhibit on the public cellular breakdown in lung WSIs dataset from The Cancer Genome Atlas (TCGA). Two datasets familiar with assess exhibit of the proposed technique: experiments on the SUCC dataset and experiments on the TCGA dataset. In [16], the technique utilized is the Finite combination model, Lung knob division based on Adaptive Particle Swarm Optimization – Gaussian blend model (APSO-GMM), the dataset have been obtained from 120 clean sound rodents, and the division impact of self-chose blended appropriation model dependent on neighbourhood data is incredible, gives reference to a clinical cellular breakdown in the lungs analysis and the limit is to expand the information limit in future to make the got results more solid. In paper [19], Several highlights, like power, wavelet, and dissipating change, are mined from the sectioned picture and given to the proposed Salp-elephant grouping advancement calculation based profound conviction organization (SEOA-DBN) for the characterization, the dataset is gathered from LIDC-IDRI, and advantages of the proposed SEOA-based DBN classifier outmatched another condition of craftsmanship procedures with the upsides of 0.96, 0.96, 0.05, and 0.0002, for precision, TPR, FPR, and FDR, separately. In [21], the creator utilized a penetrating methodology to look for anomalies, the dataset is accessed from LIDC-IDRI, and benefits are by and large, discovery affectability of the experts was 0.67 ± 0.07, while the framework accomplished 0.69. In [23], the technique utilized is a support vector machine, and recovery information is from LIDC. The advantage of the knobs of moderate size is found with 86% affectability and 91% explicitness. The pace of bogus positives per test was 0.138 for the 29 tests that were broken down. The proposed strategy is likewise a monetarily appealing arrangement since it runs on conventional PCs accessible in numerous emergency clinics. In paper [18], the proposed irregular timberlands-based order helped by grouping technique is utilized, the dataset is obtained from LIDC, and advantages are affectability of 98.33% and explicitness of 97.11% is recorded for the proposed framework. In paper [24], walking shape calculation, the vigorous mathematical model technique is utilized, the dataset is taken from 15 arbitrarily chosen people groups, and the advantage is that calculations utilized in this plan can likewise be generally effortlessly embraced as the primary discovery phase of other CAD plans.

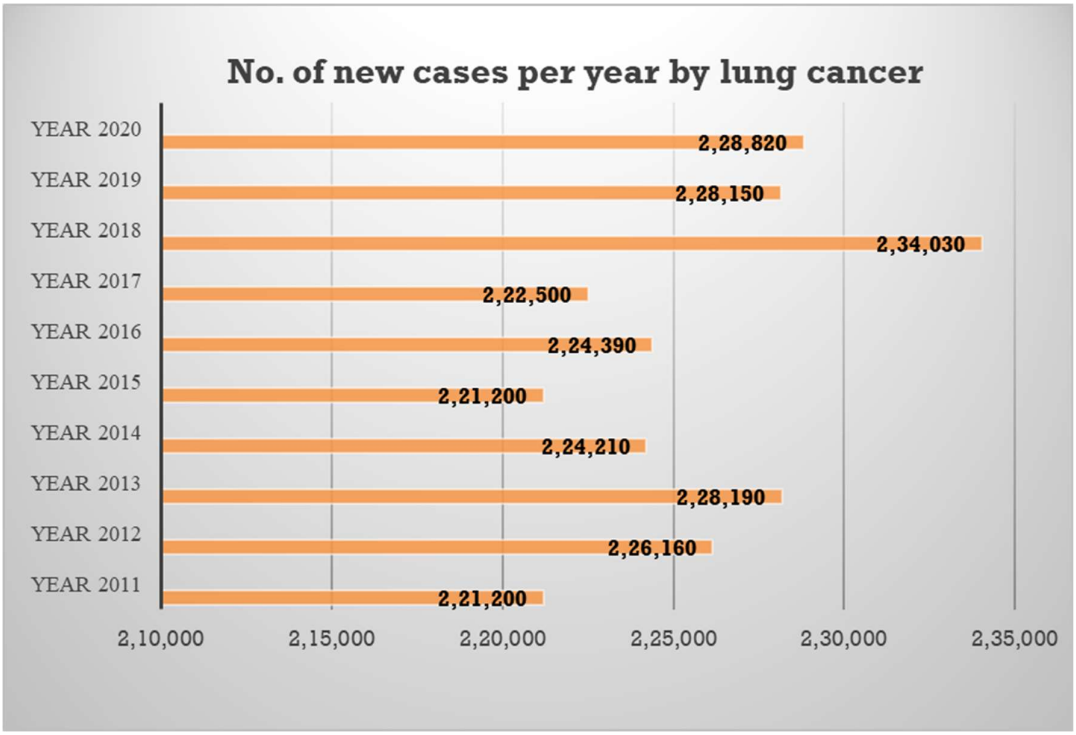

Fig. 1. No. of new cases per year by lung cancer

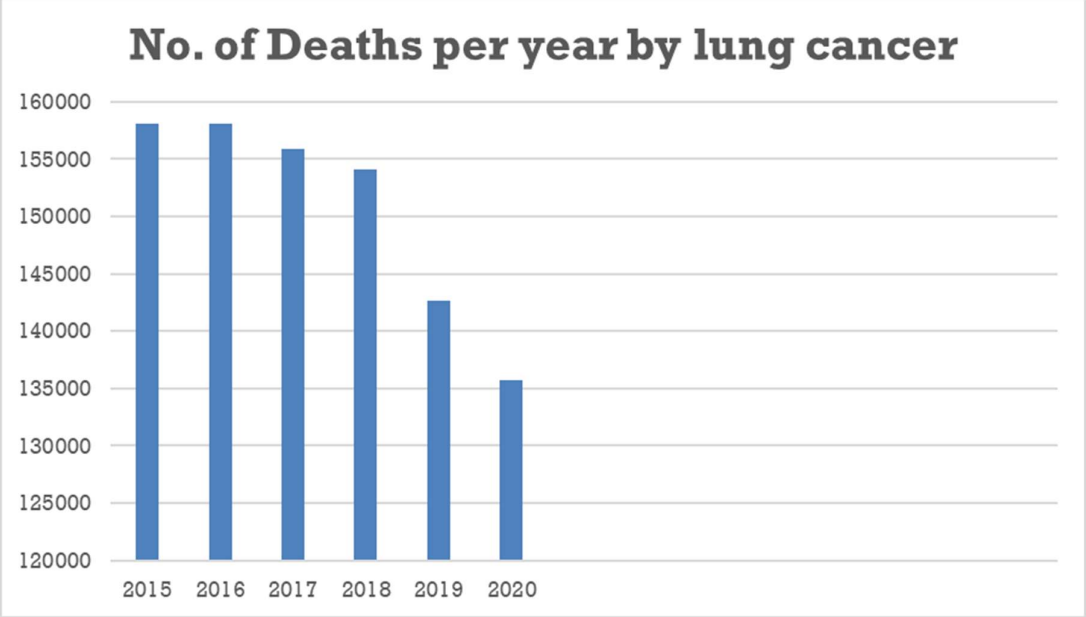

Segmentation of Lung nodule by utilizing Generative Adversarial Network

Assume, CT image dataset contains a number of CT images specified as follows,

$F = \{G_1, G_2, \ldots, G_c, \ldots, G_e\}$

(1)

Where e acts as total number of images in database, along with c^{th} image in the database is given as, G_c.

A. Gaussian filtering for pre-processing

Pre-processing is a critical step that is used to streamline the processing of CT images. The first step in pre-processing involves considering the input CT image. During this phase, artifacts present in input CT-images are eliminate. In addition, image enhancement through contrast augmentation is accomplished by applying pre-processing techniques. In the present study, a Gaussian filter is employed to eliminate noise from the CT image. Due to its noise reduction capability and ability to create smoother frequency transitions, the Gaussian filter is often used as a pre-processing step. The filter uses the two-dimensional product of the Gaussian function, which is expressed as follows:

$$K(X,Y) = \frac{1}{\sqrt{2\pi\beta^2}} e^{\frac{-X^2+Y^2}{2\beta^2}}$$

(2)

Standard deviation of the distribution, denoted by β, is utilized as a key parameter for the Gaussian filter. Filter kernel, denoted by L, has a size of both X and Y, where $(-L \le X, Y \le L)$. Following the application of the Gaussian filter, the resultant image is then processed for deep joint step.

B. Deep-Joint Segmentation for Lung Lobe Segmentation

This algorithm is designed to identify most similar regions in an image, and it accomplishes this by assessing the distance between segmentation as well as deep points [24]. This algorithm is comprised of three stages: region fusion, joining, and segmentation point generation. During the region fusion stage, the input image is divided into a grid, and the pixels within each grid are connected by estimating the threshold and mean values. Subsequently, the similarities and bi-constraints of the regions are employed to compute a new mean value through region fusion. The lowest mean values of the grid pixels are merged to score the mapped points during the region fusion stage. In the stage of segmentation point generation, the selection of optimum segments is accomplished by computing the interval between the segmentation as well as deep points, utilizing the mean squared error (MSE) as the assessment metric. The deep-joint segmentation process is initiated by splitting the pre-processed image into multiple grids. These partitioned grids are represented as follows,

$$K = \{K_1, K_2, ..., K_w, ..., K_g\}$$

(3)

Where total grids, as well as w^{th} grid in the image, are signify as g and K_w independently. During joining phase in the Deep-Joint Segmentation process, a fixed threshold value and mean values are used to connect intra-grid pixels. The mean value of each grid is computed by taking the average of the pixel values within it. Subsequently, the pixel values to be merged are chosen by applying a fixed threshold value to the mean intensity value. This pixel joining process can be expressed as:

$$K_w = \frac{\sum_{x-1}^{T} M_x}{T} \pm threshold$$

(4)

The term, $\frac{\sum_{x-1}^{T} M_x}{T}$ is utilized to calculate the mean values. In grid K_w, M_x as well as T independently represent the value and count of pixels. The third step in the Deep-Joint Segmentation process involves region fusion phase, which entails determining a region fusion matrix based on the assigned grids. To find similarities in the region, both bi-constraints and similarities in pixel intensity are used. The matrix is calculated using both bi-constraints and

similarities in pixel intensity to identify similarities between regions. The similarity within a region is determined by the following equation:

$$N_w = \frac{\sum_{q=1}^{C} M_Q^A}{P}$$

(5)

Where, joined pixel for the grid K_w in the joining phase is given as, M_Q^A and the number of joined pixels is denoted as, P. The mapping points are given as,

$$X = \{X_1, X_2, ..., X_n, ..., X_o\}$$

(6)

The fourth phase of the deep-joint segmentation process is the identification of the deep points.

$$(U) = \{M_X\}; 1 < X \le S$$

(7)

where the missed pixel as well as the pixel missed to form the connected pixel are act as follows, M_X as well as S, respectively. Finally, the deep points are determined by adding the mapped as well as missed pixels, which is shown as follows,

$$D_P = U + X_n$$

(8)

In the fifth stage, the optimum segment is determined by evaluating the deep points using an iterative procedure. Initially, segmented points y is randomly selected, and the distances between these points and the deep points are computed. The points with the smallest distance are then selected as the new segmented points, and the process is repeated until convergence. The expression for determining the minimum distance is as follows,

$$Z^{dis\tan ce} = \sqrt{\sum_{n=1}^{20} (Y_n - D_P)^2}$$

(9)

Where, the entire deep as well as segmentation points act as follows, D_P and Y_n along with iteration continues until the best-segmented points are selected based on the MSE. The Mean Squared Error (MSE) is utilized to measure the similarity between grids. During the segmentation process, if the currently segmented point is larger than the one from the previous iteration, the new point is chosen. If not, the previous segmentation points are retained. Final outcome of the lung lobe segmentation is represented by the term "I," which is then passed on to the GAN model for further segmentation.

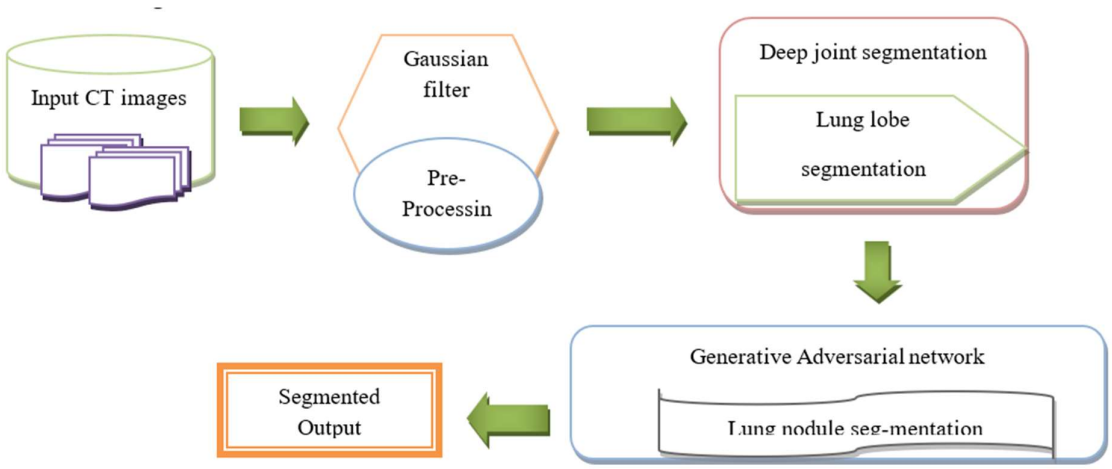

Fig. 3. Block diagram of GAN for lung nodule segmentation

Using GAN for segmenting lung nodules

This section provides an overview of the lung nodule segmentation process utilizing Generative Adversarial Networks (GANs). In essence, the GAN model is trained to accomplish the segmentation of lung nodules.

Architecture of GAN

A Generative Adversarial Network (GAN) consists of a pair of distinct models: one is a generative model (G), and the other is a discriminative model (D). The generative model can be thought of as a "forger" that aims to produce a synthetic image that is realistically similar to the actual image, in order to deceive the discriminator without being detected. A discriminative model, on the other hand, can be compared to a "policeman" trying to identify which images are fake and which are real. This competition between models continues until the generative model becomes skilled enough to produce synthetic images that can fool the discriminative model.

Some parameters and variables

Let's define some of the parameters and variables involved in the derivation.

$$
\begin{aligned}
D &= \text{Discriminator} \\
G &= \text{Generator} \\
\theta_d &= \text{Parameters of discriminators} \\
\theta_g &= \text{Parameters of generator} \\
P_z(z) &= \text{Input noise distribution} \\
P_{data}(x) &= \text{Original data distribution} \\
P_g(x) &= \text{Generated distribution}
\end{aligned}
$$

c. The process of deriving the loss function

The formula for binary cross-entropy loss can be used to derive it. Specifically, one can write the binary cross-entropy loss as follows,

$$L(\hat{y}, y) = [y.log\hat{y} + (1 - y).log(1 - \hat{y})]$$

Original data Reconstructed data

Discriminator loss

During discriminator training, data from $P_{data}(x)$ is y=1 (real data) as well as the predicted label is $\hat{y}$ = D(x). By substituting these values in the above loss function, we obtain the following result

$$L(D(x),1) = \log(D(x)) \quad (10)$$

In contrast, data generated by the generator is labeled as y = 0 (fake data), and the predicted label is $\hat{y}$ = D(G(z)). As a result, in this scenario, the following applies.

$$L(D(G(z)),0) = \log(1 - D(G(z))) \quad (11)$$

The main goal of the discriminator is to accurately differentiate between the real and fake datasets. To achieve this, we need to maximize equations (10) and (11). Therefore, the discriminator's ultimate loss function can be expressed as follows:

$$L^{(D)} = \max[\log(D(x)) + \log(1 - D(G(z)))] \quad (12)$$

d. Generator loss

As the generator competes with the discriminator, its objective is to minimize equation (12). Hence, the generator's loss function can be expressed as follows:

$$L^{(G)} = \min[\log(D(x)) + \log(1 - D(G(z)))] \quad (13)$$

e. Loss function that combines the objectives of the generator and discriminator

We can merge equations (12) and (13) into a single equation, which is:

$$L = \min_G \max_D [\log(D(x)) + \log(1 - D(G(z)))] \quad (14)$$

It should be emphasized that the aforementioned loss function is only valid for an individual data point. To account for the entire dataset, we must calculate the expectation of the equation, as shown below:

$$\min_G \max_D V(D,G) = \min_G \max_D (E_{X \sim P_{data(x)}}[\log D(x)] + E_{z \sim P_{z(z)}}[\log(1 - D(G(z)))]) \quad (15)$$

Initialization

Data used in the study have been obtained from the Lung Image Database Consortium (LIDC-IDRI) [28].

Table 1. Experimental setup

Value	Parameter
Dot per Pixels	GAN type
50	Iterations Count
1	Batch size
[16,16,1]	Disc patch
0.5	Beta 1
0.999	Beta 2
50	Epochs Count

EXPERIMENTAL RESULTS AND COMPARISON ANALYSIS

The evaluation metrics employed to analyze the various parameters are Accuracy, Dice Coefficient, and Jaccard Similarity. In the very first step, CT image is taken from the LIDC dataset. Then, the image representing the ground truth or the manually annotated version in second image, the result obtained after the pre-processing step is shown in third image, Then, the output of the lung-lobe-segmentation step, after that the output of the lung-nodule-segmentation step, and the final-image showing the segmented lung nodules.

A comparison of different segmenting lung nodules methods i.e., Kernel-based Bayesian clustering, FCM, ROI, DDRN, SVM+K-Nearest, CoLe-CNN and newly developed based on GAN.

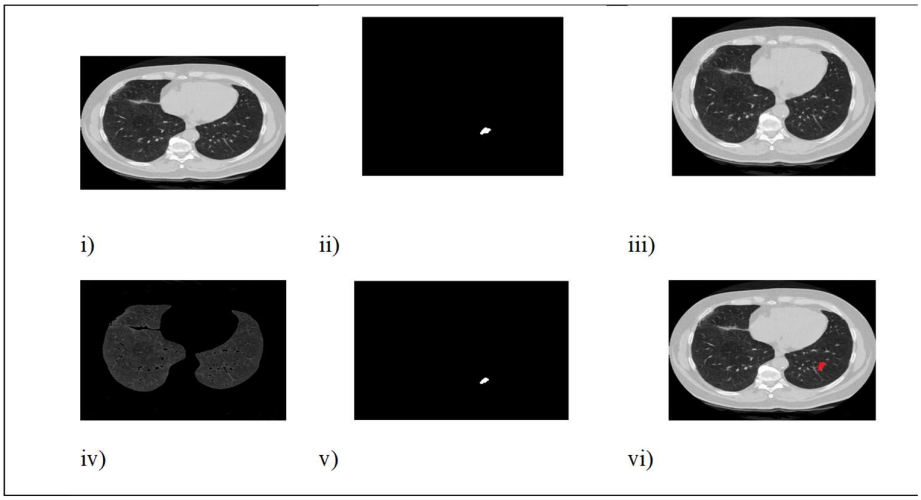

Fig. 4. i) The raw CT image of the lung, ii) The image representing the ground truth or the manually annotated version, iii) The result obtained after the pre-processing step, iv) The output of the lung-lobe-segmentation step, v) The output of the lung-nodule-segmentation step, and vi) The final-image showing the segmented lung nodules

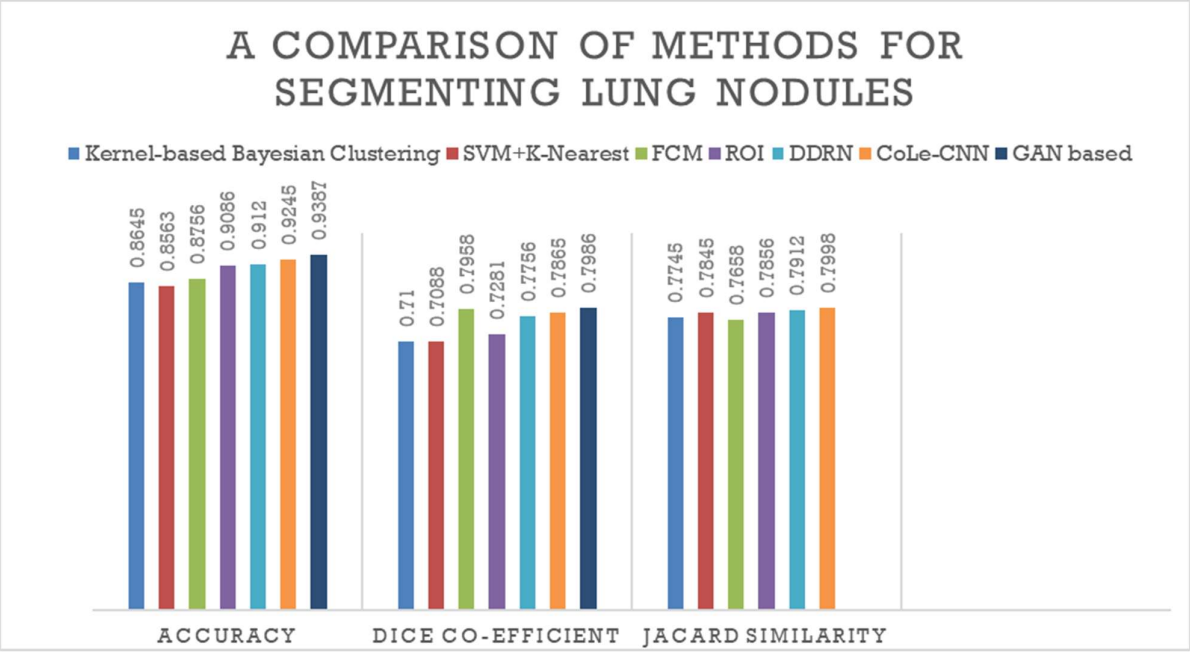

Conclusion

The study used CT images as the initial input for pre-processing, followed by denoising with a Gaussian filter. Subsequently, the pre-processed image has been segmented into lung lobes and lung nodules. A deep joint segmentation approach has been used on the pre-processed image to extract the lung lobe, with the optimal segment determined by distance measurements within the segmentation as well as deep points. Finally, the lung nodule has been segmented using GAN and efficacy has been proved.

References

[1] A. Chaudhary and S. S. Singh, "Lung cancer detection on CT images by using image processing," Proc. Turing 100 - Int. Conf. Comput. Sci. ICCS 2012, pp. 142–146, 2012, doi: 10.1109/ICCS.2012.43.

[2] H. Han, L. Li, F. Han, B. Song, W. Moore, and Z. Liang, "Fast and adaptive detection of pulmonary nodules in thoracic CT images using a hierarchical vector quantization scheme," IEEE J. Biomed. Heal. Informatics, vol. 19, no. 2, pp. 648–659, 2015, doi: 10.1109/JBHI.2014.2328870.

[3] S. Makaju, P. W. C. Prasad, A. Alsadoon, A. K. Singh, and A. Elchouemi, "Lung Cancer Detection using CT Scan Images," Procedia Comput. Sci., vol. 125, no. 2009, pp. 107–114, 2018, doi: 10.1016/j.procs.2017.12.016.

[4] M. V. A.Gajdhane and P. D. L.M, "Detection of Lung Cancer Stages on CT scan Images by Using Various Image Processing Techniques," IOSR J. Comput. Eng., vol. 16, no. 5, pp. 28–35, 2014, doi: 10.9790/0661-16532835.

[5] S. Wang et al., "Central focused convolutional neural networks: Developing a data-driven model for lung nodule segmentation," Med. Image Anal., vol. 40, pp. 172–183, 2017, doi: 10.1016/j.media.2017.06.014.
[6] D. R. Varma, "Managing DICOM images: Tips and tricks for the radiologist," Indian J. Radiol. Imaging, vol. 22, no. 1, pp. 4–13, 2012, doi: 10.4103/0971-3026.95396.
[7] S. L. A. Lee, A. Z. Kouzani, and E. J. Hu, "Random forest based lung nodule classification aided by clustering," Comput. Med. Imaging Graph., vol. 34, no. 7, pp. 535–542, 2010, doi: 10.1016/j.compmedimag.2010.03.006.
[8] Y. R. Baby and V. K. Ramayyan Sumathy, "Kernel-based Bayesian clustering of computed tomography images for lung nodule segmentation," IET Image Process., vol. 14, no. 5, pp. 890–900, 2020, doi: 10.1049/iet-ipr.2018.5748.
[9] N. Shriwash, P. Singh, S. Arora, S. M. Ali, S. Ali, and R. Dohare, "Identification of differentially expressed genes in small and non-small cell lung cancer based on meta-analysis of mRNA," Heliyon, vol. 5, no. 6, p. e01707, 2019, doi: 10.1016/j.heliyon.2019.e01707.
[10] R. Bellotti et al., "A CAD system for nodule detection in low-dose lung CTs based on region growing and a new active contour model," Med. Phys., vol. 34, no. 12, pp. 4901–4910, 2007, doi: 10.1118/1.2804720.
[11] Z. Hu, J. Tang, Z. Wang, K. Zhang, L. Zhang, and Q. Sun, "Deep learning for image-based cancer detection and diagnosis − A survey," Pattern Recognit., vol. 83, pp. 134–149, 2018, doi: 10.1016/j.patcog.2018.05.014.
[12] Y. Xie, J. Zhang, Y. Xia, M. Fulham, and Y. Zhang, "Fusing texture, shape and deep model-learned information at decision level for automated classification of lung nodules on chest CT," Inf. Fusion, vol. 42, pp. 102–110, 2018, doi: 10.1016/j.inffus.2017.10.005.
[13] J. Kuruvilla and K. Gunavathi, "Lung cancer classification using neural networks for CT images," Comput. Methods Programs Biomed., vol. 113, no. 1, pp. 202–209, 2014, doi: 10.1016/j.cmpb.2013.10.011.
[14] S. Dai, K. Lu, J. Dong, Y. Zhang, and Y. Chen, "A novel approach of lung segmentation on chest CT images using graph cuts," Neurocomputing, vol. 168, pp. 799–807, 2015, doi: 10.1016/j.neucom.2015.05.044.
[15] N. V. Keetha, S. A. P. Babu, and C. S. Rao Annavarapu, "U-Det: a Modified U-Net Architecture With Bidirectional Feature Network for Lung Nodule Segmentation," arXiv, pp. 1–14, 2020.
[16] H. Cao et al., "Dual-branch residual network for lung nodule segmentation," Appl. Soft Comput. J., vol. 86, no. xxxx, p. 105934, 2020, doi: 10.1016/j.asoc.2019.105934.
[17] G. Singadkar, A. Mahajan, M. Thakur, and S. Talbar, "Deep Deconvolutional Residual Network Based Automatic Lung Nodule Segmentation," J. Digit. Imaging, vol. 33, no. 3, pp. 678–684, 2020, doi: 10.1007/s10278-019-00301-4.
[18] S. Sharma, P. Fulzele, and I. Sreedevi, "Hybrid Model for Lung Nodule Segmentation based on Support Vector Machine and k-Nearest Neighbor," Proc. 4th Int. Conf. Comput. Methodol. Commun. ICCMC 2020, no. Iccmc, pp. 170–175, 2020, doi: 10.1109/ICCMC48092.2020.ICCMC-00034.
[19] S. Pang, Y. Zhang, M. Ding, X. Wang, and X. Xie, "A Deep Model for Lung Cancer Type Identification by Densely Connected Convolutional Networks and Adaptive Boosting," IEEE Access, vol. 8, pp. 4799–4805, 2020, doi: 10.1109/ACCESS.2019.2962862.

[20] A. A. A. Setio et al., "Pulmonary Nodule Detection in CT Images: False Positive Reduction Using Multi-View Convolutional Networks," IEEE Trans. Med. Imaging, vol. 35, no. 5, pp. 1160–1169, 2016, doi: 10.1109/TMI.2016.2536809.
[21] Y. Xiao, J. Wu, Z. Lin, and X. Zhao, "A deep learning-based multi-model ensemble method for cancer prediction," Comput. Methods Programs Biomed., vol. 153, pp. 1–9, 2018, doi: 10.1016/j.cmpb.2017.09.005.
[22] P. outcomes of nonsmall cell lung cancer using C. image Features, "Predicting outcomes of nonsmall cell lung cancer using CT image features," IEEE Access, vol. 2, pp. 1418–1426, 2014, doi: 10.1109/ACCESS.2014.2373335.
[23] G. Zhang et al., "Automatic nodule detection for lung cancer in CT images: A review," Comput. Biol. Med., vol. 103, pp. 287–300, 2018, doi: 10.1016/j.compbiomed.2018.10.033.
[24] G. Zhang et al., "Circulating Epstein-Barr virus microRNAs miR-BART7 and miR-BART13 as biomarkers for nasopharyngeal carcinoma diagnosis and treatment," Int. J. Cancer, vol. 136, no. 5, pp. E301–E312, 2015, doi: 10.1002/ijc.29206.
[25] H. Cao et al., "A Two-Stage Convolutional Neural Networks for Lung Nodule Detection," IEEE J. Biomed. Heal. Informatics, vol. 24, no. 7, pp. 2006–2015, 2020, doi: 10.1109/JBHI.2019.2963720.